ADVANCED FUNCTIONAL MATERIALS
www.afm-journal.de

Organic Photodetectors and their Application in Large Area and Flexible Image Sensors: The Role of Dark Current

Giulio Simone, Matthew J. Dyson, Stefan C. J. Meskers, René A. J. Janssen, and Gerwin H. Gelinck**

Organic photodetectors (OPDs) have gained increasing interest as they offer cost-effective fabrication methods using low temperature processes, making them particularly attractive for large area image detectors on lightweight flexible plastic substrates. Moreover, their photophysical and optoelectronic properties can be tuned both at a material and device level. Visible-light OPDs are proposed for use in indirect-conversion X-ray detectors, fingerprint scanners, and intelligent surfaces for gesture recognition. Near-infrared OPDs find applications in biomedical imaging and optical communications. For most applications, minimizing the OPD dark current density (J_d) is crucial to improve important figures of merits such as the signal-to-noise ratio, the linear dynamic range, and the specific detectivity (D^*). Here, a quantitative analysis of the intrinsic dark current processes shows that charge injection from the electrodes is the dominant contribution to J_d in OPDs. J_d reduction is typically addressed by fine-tuning the active layer energetics and stratification or by using charge blocking layers. Yet, most experimental J_d values are higher than the calculated intrinsic limit. Possible reasons for this deviation are discussed, including extrinsic defects in the photoactive layer and the presence of trap states. This provides the reader with guidelines to improve the OPD performances in view of imaging applications.

1. Introduction

1.1. Organic Photodetectors for Large Area Image Sensors

Organic photodetectors (OPDs) are increasingly attractive for light sensing applications as they combine a wide absorption spectrum and high photogeneration yield with low fabrication costs, lightweight, and flexibility.[1,2] Compared to amorphous silicon detectors, OPDs promise many important advantages, most notably that their compatibility with the thermo-mechanical properties of plastic enables large area image sensors to be solution-processed on a variety of flexible substrates.[3] By using industrially scalable coating techniques such as slot-die coating, OPD arrays can be processed from solution at a lower temperature than amorphous silicon[4] (typically less than 150 °C), thus paving the way towards lower production costs. Furthermore, to integrate OPDs in large-area image sensors, no diode patterning or alignment is required. Compared to imaging systems based on glass substrates, where refraction of light and the associated dispersion results in increased optical cross-talk between single pixels,[5] top absorbing OPD arrays with semi-transparent top electrodes enable higher resolution.

In OPDs, light is detected upon absorption of incident photons with an energy equal to or larger than the optical bandgap of the photoactive material. Due to the higher absorption coefficients of organic materials (≈10^5 cm^{-1}) when compared to silicon (50–100 cm^{-1}), thin active layers of only 100 nm are sufficient to absorb up to 60% of the incident light.[6] However, due to the lower relative permittivity ($\varepsilon_r \approx 3$–4) of organic relative to inorganic semiconductors, light absorption leads to photogenerated excitons with a comparatively high binding energy of ≈0.35–0.5 eV,[7] rather than free electrons and holes. Thus, like many organic photovoltaic (OPV) devices, the active layer of OPDs is often based on a bulk heterojunction (BHJ) architecture[8] that comprises finely intermixed percolating networks of electron donor and acceptor phases, in which their large interface area facilitates exciton dissociation while the bicontinuous networks enable charge transport to the relevant electrodes. **Figure 1**a shows a typical OPD architecture

G. Simone, Dr. M. J. Dyson, Dr. S. C. J. Meskers, Prof. R. A. J. Janssen, Prof. G. H. Gelinck
Molecular Materials and Nanosystems
Institute of Complex Molecular Systems
Eindhoven University of Technology
P.O. Box 513, 5600 MB Eindhoven, The Netherlands
E-mail: r.a.j.janssen@tue.nl; g.h.gelinck@tue.nl

Prof. R. A. J. Janssen
Dutch Institute for Fundamental Energy Research
De Zaale 20, 5612 AJ Eindhoven, The Netherlands

Prof. G. H. Gelinck
Holst Centre
TNO-The Dutch Organization for Applied Scientific Research
High Tech Campus 31, 5656 AE Eindhoven, The Netherlands

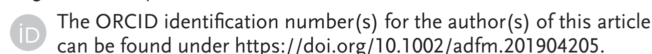
The ORCID identification number(s) for the author(s) of this article can be found under https://doi.org/10.1002/adfm.201904205.

© 2019 The Authors. Published by WILEY-VCH Verlag GmbH & Co. KGaA, Weinheim. This is an open access article under the terms of the Creative Commons Attribution-NonCommercial License, which permits use, distribution and reproduction in any medium, provided the original work is properly cited and is not used for commercial purposes.

DOI: 10.1002/adfm.201904205

comprising a BHJ layer sandwiched between electron and hole extraction layers (EEL and HEL, respectively).

1.2. Photosensor Arrays

In contrast to OPV devices that usually operate under positive bias at the maximum power point, a negative bias voltage is typically applied to OPDs (Figure 1b). For a sufficiently large reverse bias, all the photogenerated charges are efficiently extracted at the contacts due to the effective electric field, making the photocurrent independent of the applied voltage (Figure 1c).

Small OPD arrays can be read out using a so-called passive matrix.[9] In this scheme, N rows and M columns define a $N \times M$ array of photodiodes. Current sneak paths however should be considered carefully. In the passive matrix scheme, the leakage currents of all pixels at the readout line add to the signal of one pixel that is addressed. For high-resolution and large-area imaging applications, so-called active-matrix addressing is typically used. Switching elements are typically introduced in the form of thin-film transistors (TFTs), although the use of blocking diodes has also been recently proposed.[10]

In the case of a TFT active matrix, the hole extracting contacts of all photodiodes are connected to a common electrode, which is connected to an external bias voltage source. The diodes are operated with a reverse bias voltage, of typically −2 to −5 V. The electron extracting contacts of all photodiodes of each column are connected to a common readout line via a switching TFT. Each readout line is connected to the input of its assigned readout amplifier. The gates of all TFTs in each row are connected to a common gate line, which is driven by a dedicated row driver output. The flat panel sensor is scanned one row at a time, in a similar way to active-matrix displays. During one frame time all the rows are sequentially selected by applying a voltage that changes the TFTs from the non-conducting to the conducting state. In this line selection time, the readout TFT transfers the charge from the photodiode capacitance to the data line and resets the voltage across the photodiode capacitance to its original value. During this time, the charge must be transferred from the photodiode to the integrating amplifier, and the output of the amplifier must be scanned. So, all pixels of an entire line are read out simultaneously.

The negative bias voltage applied to OPD arrays when integrated with a TFT matrix[10–13] ensures that the diode remains sufficiently charged, and effectively implies that the readout charge is linearly proportional to the amount of collected photocarriers. The reverse bias also increases the response speed of the diode, and often the collection efficiency, i.e., the extraction of photogenerated charge carriers at the contacts. On the other hand, dark current density will generally increase with increasing reverse bias. A reverse bias of −2 to −5 V is typically used as a good compromise.

The flexibility of OPD arrays makes them particularly suitable for applications where conformality is desirable. An important example is X-ray detectors, well-established technologies for digital radiography in the field of medical imaging. In these indirect-conversion detectors, a scintillator layer converts X-ray photons into UV or optical photons, which are then detected by an amorphous-silicon photodetector (a-Si PD) array mounted on a rigid glass substrate (Figure 1d).[1] Replacing the a-Si PDs with solution-processed OPDs simplifies the manufacturing process considerably, thus reducing fabrication costs. Flexible X-ray image sensors remain active under deformation (Figure 1g) and easily adapt to complex shapes, thereby potentially enabling more accurate imaging of the human body than inorganic X-ray detectors based on rigid glass substrates. Ng et al.[11] first demonstrated a flexible photosensor array using solution-processed OPDs on a flexible a-Si matrix backplane. In 2014, Zhao et al.[12] proposed OPD-based X-ray imagers with amorphous indium gallium zinc oxide TFTs for next generation digital breast tomography systems. A proof-of-concept X-ray detector on thin plastic foil with 120 × 160 pixel format and 126 µm pixel size was demonstrated by Gelinck et al.[13] This

Giulio Simone is a Ph.D. student at the Eindhoven University of Technology (TU/e), The Netherlands. He received his master's degree in materials engineering and nanotechnology from the Polytechnic University of Milan. He is currently studying the device physics of organic photodetectors and their applications, for instance in artificial retinal implants and flexible pulse oximeters.

René A. J. Janssen is a professor of chemistry and physics at Eindhoven University of Technology (TU/e), The Netherlands. His current research focuses on molecular organic and hybrid semiconductors for optoelectronic applications, energy conversion, and energy storage. The work combines synthetic chemistry with optical spectroscopy, morphological characterization and the design, and fabrication and characterization of functional devices.

Gerwin H. Gelinck is a professor of applied physics at Eindhoven University of Technology (TU/e), The Netherlands. He joined Philips Research as a Senior Scientist in 1998. From 2002 to 2006, he was the Chief Scientist of Polymer Vision. Since 2007, he works at Holst Centre. His research interests include novel solution-processed semiconductors for applications in thin-film transistors and photodiodes.

© 2019 The Authors. Published by WILEY-VCH Verlag GmbH & Co. KGaA, Weinheim

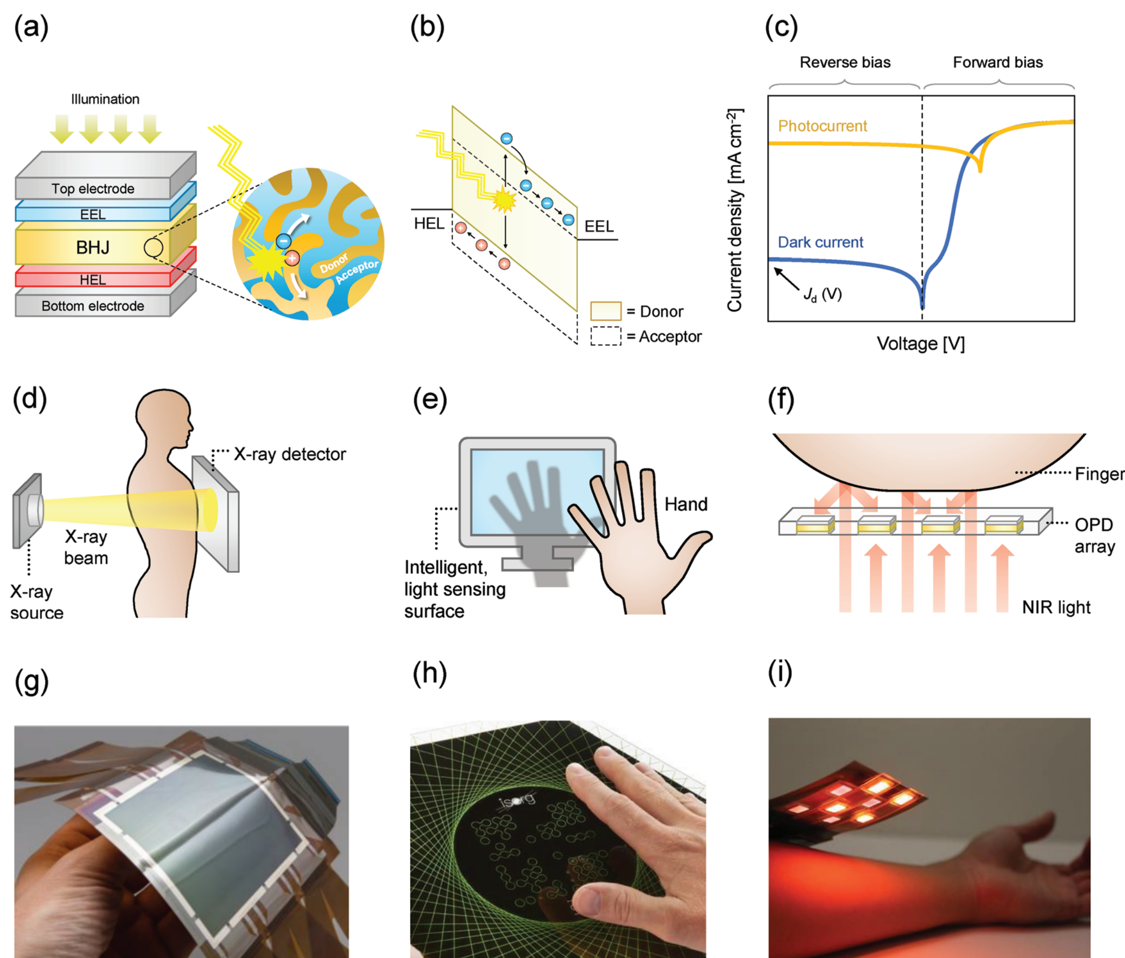

Figure 1. a) OPD architecture comprising a BHJ layer sandwiched between EEL and HEL, respectively. Charge carriers are photogenerated upon illumination through the transparent top electrode. b) Energy band diagram of OPD under reverse bias. Photogenerated excitons in the donor phase separate into free charge carriers that then drift to the respective electrodes due to the applied electric field. c) Typical OPD current density versus voltage (J–V) characteristics in a semilogarithmic plot with and without illumination, showing J_d (V) as reference value for dark current density under a given applied voltage V. d) Schematic representation of X-ray imaging using an X-ray generator and an image detector. e) Schematic representation of gesture recognition interface that detects light shadowing by the hand. f) Working principle of reflectance pulse oximeter array, where an OPD array detects NIR light reflected by the fingertip. g) Flexible large-area imager with solution-processed OPDs used for X-ray detection. g) Reproduced with permission.[19] Copyright 2019, Holst Centre. h) OPD-based arrays used to detect light shadowing for gesture recognition applications. Reproduced with permission.[20] Copyright 2019, Isorg. i) Organic pulse oximeter array to determine blood pulsation and oxygenation levels on adult forearms. Reproduced with permission.[17] Copyright 2018, National Academy of Sciences.

combined a CsI:Tl scintillator with an OPD array and an oxide TFT backplane. The OPD layer was slot-die coated directly on the active matrix backplane on thin-plastic substrate.

OPDs have also been used in prototypes of biometric fingerprint and palmprint scanners,[14,15] where the OPD array detects visible light reflected by the finger or hand, respectively, as well as for gesture recognition. Fingerprint imaging is achieved by utilizing a difference in reflectance between the finger ridges and valleys. This technology offers a low-cost alternative to bulky inorganic detectors and can be easily integrated in mobile phones or door handles. Fingerprint scanners require higher spatial resolution compared to medical X-ray applications. Typically, a resolution of 200 pixels per inch (ppi) is high enough to unlock mobile phones. However, for high-quality fingerprint authentication a higher resolution is needed, allowing for more accurate sensing and thus a greater margin of safety. For gesture recognition (Figure 1e,h), shadowing by the hand is detected using lower resolution arrays albeit of larger size. A linear photoresponse of the OPD is important for both applications, as reliable operation under a range of different light conditions is required. This can be achieved by modulating the OPD photoresponse with an additional pulsed light source and discriminating the temporal component from the time-invariant background contribution.

Another promising application for OPDs is as the fundamental light sensing element in pulse oximeters, i.e., non-invasive medical sensors that can monitor heartbeat and measure blood oxygenation.[16,17] By using near-infrared (NIR) light, the light slightly penetrates the skin and is then partly absorbed or reflected. When used in reflective mode (Figure 1f,i), organic pulse oximeters provide a versatile alternative to rigid conventional designs that typically restrict the sensing location to finger tips or ear lobes. To estimate blood oxygenation levels, a good photoresponse at ca. 850 nm is desirable.[17] Typically,

© 2019 The Authors. Published by WILEY-VCH Verlag GmbH & Co. KGaA, Weinheim

light of at least two wavelengths is sequentially emitted. By detecting the reflected light of each color, the level of arterial hemoglobin oxygenation can be assessed.

Finally, the detection of NIR radiation is attractive for a wide variety of non-medical applications as well, such as optical communication,[18] night vision, and 3D object recognition.[1] The electronic bandgap of silicon precludes light detection at wavelengths larger than ≈1100 nm, making the development of OPDs with spectral response beyond this value an interesting area for further research.

2. Performance Metrics of OPDs

Having outlined the advantages of OPDs over inorganic photodetectors, we turn to the key performance metrics that quantify suitability for specific applications. Although they have been summarized in literature,[1,2] here we provide a comprehensive definition of the most important figures of merit to enable a clear understanding of reported OPD performances. Since reported metrics are often measured using different experimental methods and conditions, direct comparison of OPD performance metrics can often generate confusion. For the most relevant metrics, we highlight the variety of experimental methods, along with their challenges or limitations, and the dependence on the main experimental parameters (e.g., bias voltage, light intensity, etc.), to increase awareness and thus promote a more critical view when comparing reported values.

2.1. EQE and Spectral Responsivity

The spectral responsivity R in units of A W^{-1} describes how much current is generated by the OPD per incoming photon of a given energy. It can be calculated via

$$R = \frac{J_{ph}}{P_{in}} \quad (1)$$

where J_{ph} is the photocurrent density and P_{in} is the incident light intensity.[1] The external quantum efficiency (EQE), i.e., the ratio between the number of incoming photons and the number of photogenerated free electrons, can be expressed as

$$\mathrm{EQE} = R\frac{h\nu}{q} \quad (2)$$

where h is the Planck constant, ν the frequency of the incident photon, and q is the elementary charge. In general, high EQE (and hence R) is desirable to ensure efficient photon flux detection. While for broad-band OPDs the EQE should ideally be spectrally invariant and as high as possible across the entire operational wavelength range, narrow-band OPDs (defined by a quasi-Gaussian spectral distribution with a full-width-at-half-maximum (FWHM) ≤ 100 nm) that require color discrimination should display high EQE only within the desired spectral window.[1] In addition to input filtering, the EQE spectrum can be manipulated by accurately tuning the optical bandgap, and hence absorption properties of the donor and acceptor phase. An alternative approach employs a thick (≈2 µm) BHJ layer to induce charge collection narrowing, in which only weakly absorbed photons produce electrons sufficiently close to the EEL to be collected.[21] Further increase of the EQE in specific wavelength ranges can be obtained by exploiting microcavity effects.[22,23] Since heterojunction OPDs behave as thin film optical cavities, interference phenomena derived from multiple reflections between two metallic semitransparent electrodes can enhance absorption within the photoactive layer, leading to broadening or narrowing of certain spectral features. These effects can be manipulated by carefully tuning the photoactive layer thickness and the properties of the optical spacer layers, and have recently been employed to enhance the EQE in the infrared region by increasing the charge-transfer (CT) state absorption.[24] EQE can also be enhanced by photomultiplication, i.e., the collection of multiple charge carriers per incident photon. In OPDs, this is generally achieved when trapped charge carriers cause the energy bands to bend, resulting in enhanced charge injection under illumination.[25]

Finally, EQE (and hence R) under reverse bias generally increases with greater applied voltage (i.e., electric field strength) due to enhanced charge extraction efficiency, but should eventually reach the saturation limit. In contrast, the dark current density (J_d) will keep increasing with increasing electric field (see Section 5.1), implying a trade-off between high EQE and low J_d under reverse bias.

2.2. Speed of Response

Once electrons and holes are generated upon photon absorption, they drift towards the relevant electrodes due to the applied electric field. The speed of response, defined as the time required to collect photogenerated charge carriers at their respective contacts, ultimately determines the OPD dynamic range and cut-off frequency.[26] The response time can be measured by various techniques, including time-of-flight photocurrent transients[27] or small perturbation methods such as impedance spectroscopy.[28] Although they probe similar phenomena, these techniques may lead to different experimental results at low charge carrier densities ($<10^{16}$ cm^{-3}) due to surface recombination at the electrodes or inhomogeneous charge distribution across the active layer.[29] For polymer:fullerene BHJ OPDs, it is widely accepted that the transit time is limited by the mobility of the slowest carrier,[30] usually attributed to holes in the polymer phase.[31] Transit times for typical OPDs with thicknesses of 100–300 nm are of the order of µs, still less than the shortest interframe time (33 ms) for imaging applications operating at 30 frames per seconds (fps).[30]

2.3. Noise equivalent power and specific detectivity (D^*)

The minimum incident light power that can be detected by the OPD is referred to as noise equivalent power (NEP). The NEP is also defined as the signal optical power yielding a signal-to-noise ratio (SNR) equal to 1.[2] Making use of the definition for the spectral responsivity given by Equation (1), the NEP in units of W $Hz^{-1/2}$ can be expressed as

$$\mathrm{NEP} = \frac{i_{noise}}{R\sqrt{B}} \quad (3)$$

where i_{noise} is the noise current and B the detection bandwidth.[1] The specific detectivity D^* in units of cm $Hz^{1/2}$ W^{-1}

© 2019 The Authors. Published by WILEY-VCH Verlag GmbH & Co. KGaA, Weinheim

(i.e., Jones) is the reciprocal of the NEP normalized to the square root of the device area A:

$$D^* = \frac{R\sqrt{AB}}{i_{\text{noise}}} \tag{4}$$

Although accurate determination of i_{noise} is essential to estimate D^*, experimental measurements of i_{noise} are challenging and not always performed. For sake of simplicity, the shot noise i_{shot} from the dark current i_d is often assumed to be the dominant contribution to i_{noise}, leading to

$$D^* \cong \frac{R\sqrt{AB}}{i_{\text{shot}}} = \frac{R\sqrt{A}}{\sqrt{2qi_d}} = \frac{R}{\sqrt{2qJ_d}} \tag{5}$$

Under this assumption, J_d is taken to be a constant value that is subtracted from the photoinduced signal. The use of Equation (5) implies that the dark current is dominated by shot noise that limits D^*, while $1/f$ noise and thermal noise[32] are ignored. It has been pointed out that this assumption can overestimate the specific detectivity.[1,33] The general applicability of Equation (5) can therefore be questioned. However, Equation (5) is widely used and thus enables a fair comparison between reported OPD performances. Nevertheless, confusion may still arise when comparing reported D^* calculated with Equation (5), for two reasons: a) J_d depends on the applied electric field (see Section 5.1) and b) R depends on the wavelength and the applied light intensity according to Equation (1). Because it is not always possible to compare D^* values measured under the same experimental conditions, here we will consider the maximum D^* value reported in each work.

2.4. Dark Current Density (J_d)

Dark current is defined as any current generated under an applied reverse bias voltage in the absence of light. The detrimental influence of a high dark current density on OPD performance can be quantified by its negative impact on several key metrics. First, high J_d results in a lower SNR and decreases sensitivity to low light intensities. Furthermore, it constrains the linear dynamic range (LDR), i.e., the operational light intensity range of the image sensor,[1] by increasing the minimum detectable photocurrent. Finally, the specific detectivity D^* decreases for increasing dark current densities according to Equation (5). Unlike R, J_d can span multiple orders of magnitude depending on material properties and device architecture,[34] meaning that reducing J_d is of utmost importance for improving SNR, LDR, and D^* in OPDs. Exploration of the origins of dark current, so essential to minimize when developing high-performing OPDs, and specific strategies to reduce J_d form the bulk of this progress report.

Over recent years, great effort has been devoted to lowering dark current density in OPDs. State-of-the-art OPDs exhibit values in the range of 10^{-6}–10^{-7} mA cm^{-2}.[5,34,35] However, direct comparison of the reported values is sometimes hampered by the fact that J_d can strongly depend on the applied bias, and no specific measurement protocol is agreed. To avoid confusion, in this work we report J_d values at a given effective electric field $F = 6 \times 10^6$ V m^{-1}, unless otherwise stated. This field corresponds to an applied voltage of $V = -2$ V over an active layer with a thickness $L = 300$ nm (assuming $F = V/L$), and thus falls into a reasonable range for OPD applications.

3. Dark Current in OPDs: Origin and Solutions

3.1. Dark Current Mechanisms

Effective suppression of OPD dark current requires a deep understanding of its fundamental origin. When the OPD is operated under an applied reverse bias voltage, intrinsic J_d (i.e., in the absence of pinholes or other extrinsic leakage phenomena) is mainly attributed to the charge carrier injection rate from the contacts into the semiconductor, or the rate of thermal generation of charge carriers within the bulk of the active layer, followed by drift towards their respective electrodes under the applied electric field. In **Figure 2**a, the energy levels of donor and acceptor are represented by the orange full lines and the black dotted lines, respectively. The density of state (DOS) distributions of the donor highest occupied molecular orbital (HOMO) and the acceptor lowest unoccupied molecular orbital (LUMO) are assumed to be Gaussian.

In the first scenario, electrons are injected from the high work function electrode into energy states in the tail of the Gaussian DOS of the acceptor LUMO, whereas holes are injected from the low work function electrode into tail states of the donor HOMO. The charge injection rate is expected to be strongly dependent on the injection barrier Φ_b, defined as the energy difference between the acceptor LUMO and Fermi level of the high work function electrode in the case of electrons. A higher Φ_b results in a lower dark current for a given applied bias. Assuming perfect Ohmic contacts and alignment between the low (high) work function electrode Fermi level and the acceptor LUMO (donor HOMO), the injection-limited J_d is expected to be proportional to the effective bandgap E_g, defined as the energy difference between the acceptor LUMO and the donor HOMO, as donor and acceptor materials are in contact with both electrodes.

In the second scenario, charge carriers are thermally generated and collected at the contacts. It is often stated that bulk thermal generation within the polymeric semiconductor can be neglected due to the large bandgap E_0 of organic materials (i.e., $E_0 > 1$ eV),[2] resulting in negligibly small concentration of thermally generated carriers (n_i), as $n_i \propto \exp(-E_0/k_BT)$ with k_B the Boltzmann constant and T the absolute temperature. However, thermally generated carriers close to the donor–acceptor (D-A) interface might be easily dissociated within the effective bandgap E_g, leading to $n_i \propto \exp(-E_g/k_BT)$. Although thermal generation at the D-A interface via ground-state CT interaction can typically be neglected in the case of UV–visible OPDs[2,36] due to the deep HOMO energy of the donor material resulting in large E_g, its contribution may be relevant for NIR-sensitive OPDs.

3.2. Dark Current Reduction Strategies

Figure 2b summarizes the main experimental approaches to reduce the dark current density in OPDs. First, J_d can be reduced by astute selection of the energy levels within the

© 2019 The Authors. Published by WILEY-VCH Verlag GmbH & Co. KGaA, Weinheim

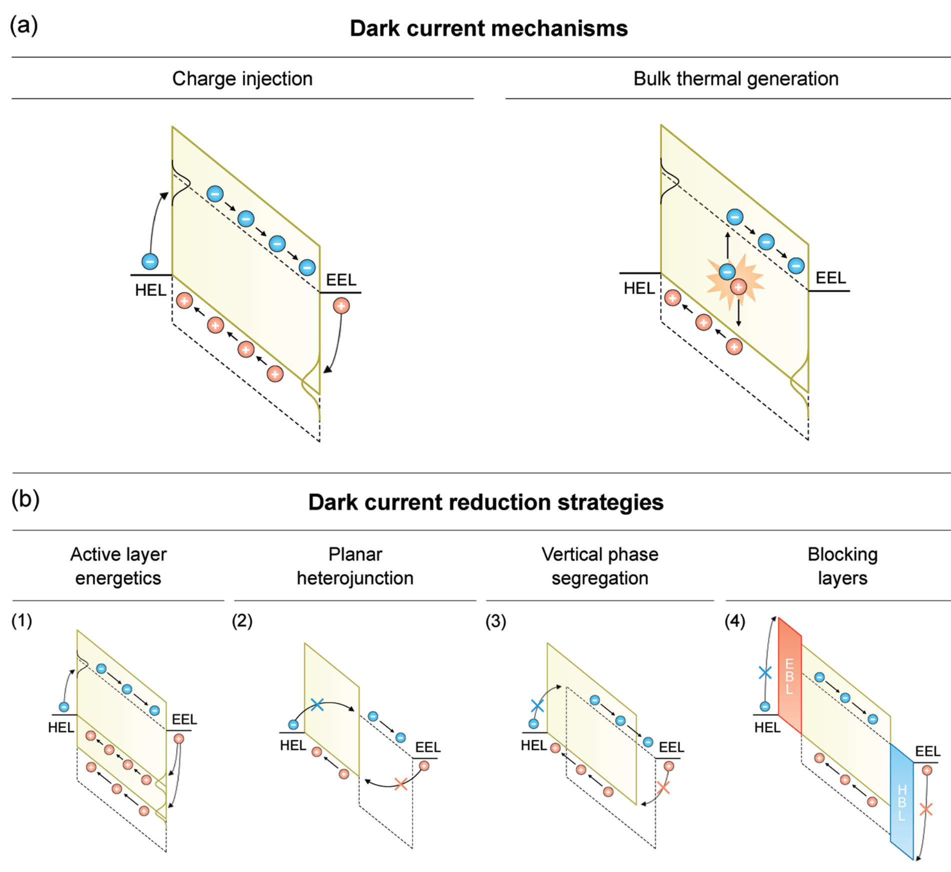

Figure 2. a) Dark current mechanisms: charge injection from the contacts into tail states of the Gaussian DOS and bulk thermal generation of charge carriers within the active layer. b) Main strategies to achieve dark current reduction: 1) a deep HOMO energy of the donor increases the energetic barrier for hole injection; 2) a PHJ architecture, 3) vertical phase segregation both reduce charge injection from both electrodes; and 4) blocking layers increase the energetic barrier for charge carrier injection.

photoactive layer. Choosing a donor material with a deep HOMO energy would minimize hole injection from the low work function electrode (see Section 4.1). Equally, an acceptor material with a shallow LUMO would be expected to minimize electron injection, but this route is less explored as most OPD are developed using fullerene derivatives with similar LUMO values.[37] Furthermore, donor and acceptor materials with smaller energetic disorder, i.e., a narrower Gaussian DOS, are expected to increase the effective injection barrier, thereby reducing J_d.

In addition, the photoactive layer stratification can be adjusted specifically with the aim of reducing the dark current density (see Section 4.2). Planar heterojunction (PHJ) OPDs made via sequential deposition of individual donor and acceptor layers are widely investigated.[38,39] Alternatively, sequentially solution-processed (SSP) OPDs[40,41] can lead to a partial donor-acceptor interpenetration, resulting in a well-mixed interdiffusion phase in the middle of the bulk. Both approaches can lead to the formation of pure phases at the electrodes, which can effectively block unfavorable charge carrier injection under reverse bias. The injection barrier Φ_b, and thus the charge injection rate is expected to scale with the energy difference between the donor LUMO and Fermi level of the high work function electrode in the case of electrons.

Another common strategy to reduce J_d consists of improving charge selectivity at the contacts (see Section 4.3). This is obtained by raising energetic barriers to charge injection under reverse bias, while maintaining an energy cascade between the active layer and the corresponding electrodes to facilitate extraction of photogenerated carriers.[42] To achieve this, electron-blocking layers (EBLs) and hole-blocking layers (HBLs) are often employed. These comprise an additional interlayer between the electrode and the photoactive layer, such that $E_{LUMO,EBL} > E_{LUMO,acceptor}$ for electrons and $E_{HOMO,HBL} < E_{HOMO,donor}$ for holes, resulting in an increased energetic barrier for charge injection. Ideally, $E_{HOMO,EBL} = E_{HOMO,donor}$ and $E_{LUMO,HBL} = E_{LUMO,acceptor}$ so that photogenerated carrier collection is not impeded.

Table 1 contains a summary of recently published OPD performances. In each work, J-V characteristics in dark conditions and/or D^* spectra are presented, the main J_d mechanisms are mentioned and/or a description of the experimental approach for J_d reduction is provided, along with the experimental results. J_d values are chosen at electric field $F = 6 \times 10^6$ V m^{-1}. $D^*(\lambda_{max})$ is the specific detectivity at the wavelength corresponding to the maximum of the first allowed optical absorption band of the semiconductor. Reported D^* values were calculated using Equation (5), unless otherwise stated. Interestingly, fullerene derivatives are used as electron acceptors in all work, except for

© 2019 The Authors. Published by WILEY-VCH Verlag GmbH & Co. KGaA, Weinheim

Table 1. Overview of the most common J_d mechanisms and experimental approaches for J_d reduction. Dark current density (J_d) and specific detectivity (D^*) at the wavelength corresponding to the maximum of the first allowed optical absorption band of the semiconductor (λ_{max}).

Year	Ref.	J_d mechanism		Experimental approach for J_d reduction				Results		
		Charge injection	Bulk thermal generation	Active layer materials[a)]	Active layer morphology	Blocking layers		J_d [mA cm^{-2}][b)]	$D^*(\lambda_{max})$ [Jones]	λ_{max} [nm]
						EBL[a)]	HBL[a)]			
2007	[44]	✓	–	P3HT:$PC_{61}BM$	BHJ	PFB	–	2.0×10^{-4}	–	500
2008	[45]	✓	–	P3HT:$PC_{61}BM$	BHJ	–	–	5.0×10^{-6}	7.0×10^{12}	468
2011	[46]	✓	–	Squaraine:$PC_{61}BM$	BHJ	MEH-PPV	–	3.5×10^{-6}	3.4×10^{12}	700
2012	[47]	✓	–	P3HT:$PC_{61}BM$	BHJ	–	TAZ	4.5×10^{-5}	3.0×10^{12}	500
2013	[48]	✓	–	C_{60}	Single layer	C-TPD	–	7.0×10^{-6}	3.6×10^{11}	370
2013	[49]	✓	–	P3HT:$PC_{61}BM$	BHJ	P3HT	–	3.0×10^{-6}	–	600
2013	[50]	✓	–	PBDTTT-C:$PC_{71}BM$	BHJ	–	PEIE	2.0×10^{-6}	8.5×10^{12}	680
2015	[51]	✓	–	P3HT:Indigo	BHJ	–	–	2.9×10^{-5}	1.0×10^{12}	630
2015	[35]	✓	–	PDPP3T:$PC_{71}BM$	BHJ	poly-TPD	–	1.0×10^{-6}	1.0×10^{13}	870
2015	[52]	✓	–	PCDTBT:$PC_{71}BM$	BHJ	–	PEIE	1.4×10^{-7}	3.4×10^{13}	532
2016	[13]	✓	–	PCDTBT:$PC_{61}BM$	BHJ	–	–	7.0×10^{-8}	3.0×10^{13}	575
2016	[53]	✓	–	P3HT:$PC_{61}BM$	BHJ	poly-PT	–	2.5×10^{-5}	2.2×10^{12}	505
2016	[54]	✓	–	PVK:$PC_{71}BM$	BHJ	TAPC	–	3.5×10^{-4}	5.6×10^{12}	350
2016	[34]	✓	–	PCDTBT:$PC_{71}BM$	BHJ	–	PEIE	3.0×10^{-7}	3.2×10^{13}	528
2016	[55]	✓	–	P3HT:$PC_{61}BM$	BHJ	–	YbF_3	–	1.7×10^{12}	520
2016	[56]	✓	–	P3HT:$PC_{61}BM$	BHJ	–	C_{60}	1.3×10^{-5}	2.4×10^{12}[c)]	580
2016	[38]	✓	–	ZnO:F8T2	PHJ	–	–	6.0×10^{-7}	1.2×10^{12}[c)]	450
2017	[42]	✓	–	PBDTT-FTTE:$PC_{71}BM$	BHJ	–	–	1.5×10^{-5}	3.3×10^{12}[c)]	690
2017	[57]	✓	✓	P3HT:$PC_{61}BM$	BHJ	–	–	1.0×10^{-5}	–	–
2017	[39]	–	✓	TAPC:C_{60}	PHJ	–	–	6.5×10^{-7}	–	–
2017	[58]	–	–	P3HT:$PC_{60}BM$	BHJ	–	–	3.0×10^{-5}	2.5×10^{12}[c)]	650
2017	[59]	–	–	PFBT2OBT:$PC_{71}BM$	BHJ	–	–	1.3×10^{-6}	1.0×10^{13}	530
2018	[60]	✓	–	PIDT-TPD:$PC_{61}BM$	BHJ	TIPS-P	–	1.0×10^{-6}	1.4×10^{13}	610
2018	[41]	✓	–	P3HT:$PC_{71}BM$	SSP	–	–	2.0×10^{-4}	1.2×10^{12}	530
2019	[61]	✓	–	C_{60}	Single layer	TAPC	–	3.5×10^{-7}	6.4×10^{12}	360
2019	[5]	✓	✓	PV-D4650:$PC_{61}BM$	BHJ	–	–	3.4×10^{-8}	2.2×10^{13}[c)]	660
2019	[43]	–	–	P3HT:O-IDTBR	BHJ	–	–	2.0×10^{-5}	4.6×10^{12}	755

[a)]Abbreviations are defined in the text; PFB = poly[9,9′-dioctylfluorene-co-bis-N,N′-(4,butylphenyl)-bis-N,N′-phenyl-1,4-phenylene-diamine]; MEH-PPV = poly[2-methoxy-5-(2′-ethyl-hexyloxy)-1,4-phenylene-vinylene]; TAZ = 3-phenyl-4(1′-naphthyl)-5-phenyl-1,2,4-triazole; C-TPD = cross-linked 4,4′-bis[(p-trichlorosilylpropylphenyl)-phenylamino]-biphenyl; PVK = poly(9-vinylcarbazole) and F8T2 = poly(9,9-dioctylfluorene-alt-bithiophene); F8T2 = poly(9,9-dioctylfluorene-alt-bithiophene); PIDT-TPD=poly-[4,4,9,9-tetrakis(4-hexylphenyl)-4,9-dihydro-s-indaceno[1,2-b:5,6-b′]dithiophene-2,7-diyl-alt-5-(2-ethylhexyl)-4H-thieno-[3,4-c]pyrrole-4,6(5H)-dione-1,3-diyl];TIPS-P = 6,13-bis-(triisopropylsilylethynyl)pentacene; O-IDTBR = rhodanine-benzothiadiazole-coupled indacenodithiophene; [b)]J_d at reverse bias electric field $F = 6 \times 10^6$ V m^{-1}; [c)]D^* values based on experimental measurements of the noise current i_{noise}.

some recent exceptions.[38,43] This implies that the difference in optical and electrical characteristics reported here are largely due to the different polymers used as donor materials. Furthermore, dark current densities below ≈ 10^{-7} mA cm^{-2} are rarely achieved within a relevant electric field range for applications. Nevertheless, very low J_d in the order of 10^{-7} mA cm^{-2} can be obtained using various methods, which suggests that there is currently no unique strategy to reduce the dark current density in OPDs. This indicates that J_d depends in a complex way on several material and design parameters, and that its underlying mechanisms are still largely unknown.

Figure 3 shows a graphical overview of OPDs reported in the recent years. In Figure 3a, the dark current density at reverse bias electric field $F = 6 \times 10^6$ V m^{-1} is plotted as function of the wavelength corresponding to the maximum of the first allowed optical absorption band of the polymeric semiconductor. Here, OPDs are classified in four categories according to the wavelength of operation, namely UV, blue, green, and NIR, with the clear majority lying in the region between 500 and 700 nm. Although the lowest dark currents are generally reached for wide bandgap materials, there is no evident correlation between J_d and λ_{max}. Adding blocking layers

© 2019 The Authors. Published by WILEY-VCH Verlag GmbH & Co. KGaA, Weinheim

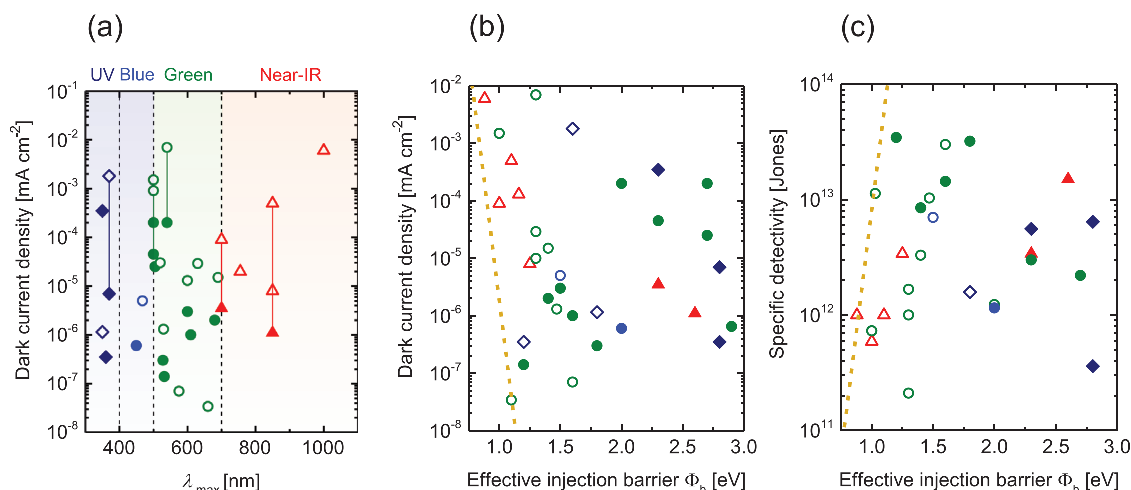

Figure 3. Overview of recently published OPD parameters (for details see Figures S1–S3, Supporting Information). Empty symbols refer to BHJ OPDs without BLs, full symbols refer to BHJ OPDs with BLs or PHJ OPDs. a) Dark current density at a reverse bias electric field $F = 6 \times 10^6$ V m^{-1} as function of wavelength corresponding to the maximum of the first allowed optical absorption band of the semiconductor. Symbols linked by full lines belong to the same publication. b) Dark current density at reverse bias electric field $F = 6 \times 10^6$ V m^{-1} and c) maximum specific detectivity D^* as function of the effective bandgap, i.e., the difference between the acceptor LUMO and the donor HOMO. The dashed line in b) indicates the instrinsic limit of the injection-limited J_d as calculated from Equation (7) for a reference OPD, as explained in Section 5.1. The dashed line in c) was determined using Equation (5) with the calculated J_d and assuming $R = 0.2$.

(full symbols) clearly helps reducing J_d while maintaining the same OPD spectral response. In the case of NIR OPDs, BLs seem to be essential to achieve low dark current densities in the order of 10^{-6} mA cm^{-2}. However, green-sensitive OPDs with blocking layers still do not outperform the best BHJ OPDs without BLs at the same operational wavelengths. In the attempt to plot J_d in a meaningful way for OPDs with and without BLs, Figure 3b shows J_d as function of the effective injection barrier Φ_b. For OPDs with Ohmic contacts, $\Phi_b = E_g = |\text{LUMO}_A - \text{HOMO}_D|$ assuming pinning of the BHJ energy levels to the work function of the injecting contacts under reverse bias, as explained in Section 3.1. For OPDs with electron or hole BLs, $\Phi_b = |\text{LUMO}_{EBL} - W_e|$ or $\Phi_b = |W_h - \text{HOMO}_{HBL}|$, respectively, with $W_{e,h}$ the work function of the electron or hole injecting contact under reverse bias. Finally, for OPDs with PHJ active layers, $\Phi_b = |\text{LUMO}_A - W_e|$ or $\Phi_b = |W_h - \text{HOMO}_D|$ for the case of electron or hole injection under reverse bias, respectively. The dashed line indicates the instrinsic limit of the injection-limited J_d as calculated from Equation (7) for a reference OPD, as explained in Section 5.1. Here, the absolute values of LUMO_A and $\text{HOMO}_{D,}$ as well as the energy levels of the BLs and the work functions of the injecting contacts under reverse bias, were taken from each work; uncertainty regarding their absolute values that arises from different measuring techniques must be considered, as will be discussed in Section 6. Nevertheless, it becomes clear that low dark current densities can rarely be achieved when the effective injection barrier is reduced, due to the enhanced probability of charge carrier injection and/or bulk thermal generation. This also sets an intrinsic limit to the maximum D^* for small values of Φ_b (Figure 3c). Here, the intrinsic limit of D^* was assessed with Equation (5) using the calculated J_d and assuming a reasonable value for the responsivity R, i.e., $R = 0.2$. While the use of BLs in many works decreases J_d (increases D^*), most results are scattered and still lie far from the intrinsic limits for a given value of Φ_b. This suggest that BLs can effectively lower the dark current but do not reduce J_d to the expected intrinsic limit. In addition, this indicates that extrinsic factors may affect the experimental values of J_d and D^* in many cases. Possible explanations for this are the object of further discussion in Section 6. Notably, the graphical overview in Figure 3b enables to identify the best reported OPDs (data points approaching the intrinsic limits), some of which are object of a more detailed study in Section 4.

4. Effect of OPD Parameters on Dark Current

In this section, we provide a more detailed analysis to the different experimental approaches employed to reduce the OPD dark current. For each approach, the best examples of OPDs in literature are cited and their J_d values are reported, with the aim to select the most successful strategies for J_d reduction.

4.1. Active Layer Energetics

Having a large offset between the Fermi level of the electron extracting contact and the donor polymer HOMO energy has been reported to be a prerequisite to reduce hole injection and thus minimize J_d. Indeed, the lowest dark current densities reported in literature for OPDs are achieved using polymers with a deep HOMO energy. It is no coincidence that the record values of J_d are achieved for poly[*N*-9′-heptadecanyl-2,7-carbazole-alt-5,5-(4′,7′-di-2-thienyl-2′,1′,3′-benzothiadiazole)] (PCDTBT),[34,52] which has one of the deepest HOMO energies amongst photovoltaic polymers (≈ 5.5 eV).[34] This implies that careful selection of the photoactive layer materials is a key element to reducing J_d without additional interlayers, resulting in a faster and cheaper fabrication process. However, a trade-off between J_d and the maximum absorption wavelength of the photoactive layer is

© 2019 The Authors. Published by WILEY-VCH Verlag GmbH & Co. KGaA, Weinheim

reached, given the need for a suitably shallow donor polymer LUMO that facilitates exciton separation under illumination and ensures a high open circuit voltage (V_{oc}). If the LUMO of the donor is too deep, this would cause inefficient exciton separation and thus low responsivity.[62] Optimal energetic offset in the order of ≈ 0.2–0.3 eV is necessary to achieve CT from donor to acceptor.[63] It must be emphasized that this rule is empirical and that exceptions may occur where efficient free charge carriers are photogenerated even at lower energy offsets. Nevertheless, this requirement sets an intrinsic limitation to the deepest HOMO energy for NIR polymers, where a narrow optical bandgap must be maintained to enable the detection of the NIR radiation. As an example, assuming light absorption mainly in the donor phase and 0.25 eV LUMO offset relative to the acceptor, an effective bandgap E_g of ≈ 1.1 eV is necessary to detect light up to 850 nm for applications in pulse oximeters (see Section 1.2). The relatively low E_g of NIR OPDs enhances charge injection from the metal electrodes—assuming Ohmic contacts between the electron (hole) extracting layer and the LUMO of the acceptor (HOMO of the donor)—or thermal generation within the photoactive layer. This makes it challenging to achieve NIR-sensitive OPDs with low J_d and high D^* by only optimizing the photoactive layer energetics.

4.2. Optimization of the Photoactive Layer: Stratification and Thickness

The PHJ architecture provides a valid approach to reduce the injection-limited as well as the thermally generated J_d. Recently, Yoon et al.[38] achieved $J_d = 6 \times 10^{-7}$ mA cm^{-2} at $F = 6 \times 10^6$ V m^{-1} for a color-selective inverted-polarity PHJ OPD using a blue-sensitive polymer donor in combination with non-absorbing ZnO acceptor. Shekhar et al.[39] reached J_d in the order of 10^{-6} mA cm^{-2} in combination with EQE well above 10% in the spectral range between 400 and 800 nm. This promising result was obtained using very thin donor and acceptor layers [20 nm of boron subphthalocyanine chloride (SubPc) and 40 nm of C_{70}, respectively] to ensure fast migration of the photogenerated exciton to the D-A interface and efficient charge separation.

Agostinelli et al.[40] investigated the effect of D-A vertical segregation on the dark current density of a SSP OPD based on poly(3-hexylthiophene) (P3HT) and phenyl-C_{61}-butyric acid methyl ester ($PC_{61}BM$). Changes in the vertical composition profile induced by annealing led to better contact selectivity that reduced J_d under reverse bias. However, the OPD with the lowest J_d (≈ 10^{-8} mA cm^{-2}) also showed a relatively low EQE of 0.024 at 500 nm, mainly attributed to the high series resistance of the thick $PC_{61}BM$ layer and the inefficient separation of photogenerated excitons due to insufficient interdiffusion at the P3HT-$PC_{61}BM$ interface. In the work of Wang et al.,[41] optimal interdiffusion of at the D-A interface led to high EQE of 0.69, but J_d did not decrease below 10^{-4} mA cm^{-2} at $F = 6 \times 10^6$ V m^{-1}. Thus, the trade-off between EQE and dark current density depending on the degree of D-A vertical segregation is the main limitation of SSP OPDs.

Finally, J_d is found to decrease with increasing photoactive layer thickness L for two main reasons, namely 1) the decrease of extrinsic defects[64] (e.g., film imperfections, pinholes, and other leakage paths) resulting in higher manufacturing yields and lower probability of soft breakdown above a certain electric field, and (2)) the reduction of image charge effect,[65] resulting in a higher effective barrier for charge injection. Biele et al.[5] optimized the spray coating process anticipated by Tedde et al.[66] by using high boiling point 1,8-diiodooctane (DIO) as processing additive, which enabled the single droplets to coalesce, resulting in a thick active layer (800 nm) with reduced root-mean-square roughness. This led to an impressively low dark current density of $J_d = 3.4 \times 10^{-8}$ mA cm^{-2} and EQE = 0.82 at 650 nm under −5 V (**Figure 4**). Pierre et al.[52] reported high manufacturing yields for OPDs with the maximum thickness limited by the solubility of donor and acceptor phases in solution (≈ 570 nm). On the other hand, too thick active layers (≈ 1000 nm) cause a decrease in responsivity as charge carriers are not efficiently extracted and thus recombine within the photoactive layer.[5] This implies a trade-off between J_d and photocurrent as L is varied.[67]

4.3. Improving the Charge Selectivity at the Contacts

4.3.1. Electron-Blocking Layers

In the recent years, many groups have employed EBLs to effectively reduce the dark current in OPDs. Zhou et al.[35]

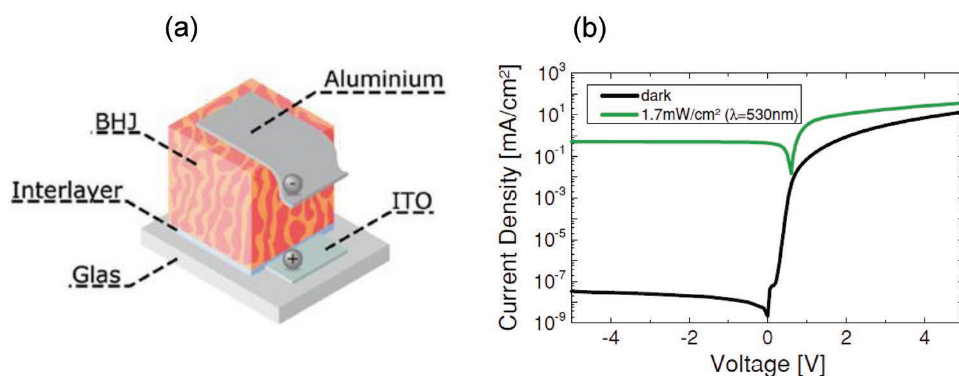

Figure 4. Effect of active layer thickness on J_d in BHJ OPDs. a) Lisicon PV-D4650:$PC_{61}BM$ OPD architecture. A thick active layer with L = 800 nm is employed. b) J–V characteristics in dark conditions and under illumination for the spray coated OPD with DIO cosolvent and 800 nm active layer thickness. Reproduced with permission.[5] Copyright 2019, Wiley-VCH Verlag GmbH & Co. KGaA.

© 2019 The Authors. Published by WILEY-VCH Verlag GmbH & Co. KGaA, Weinheim

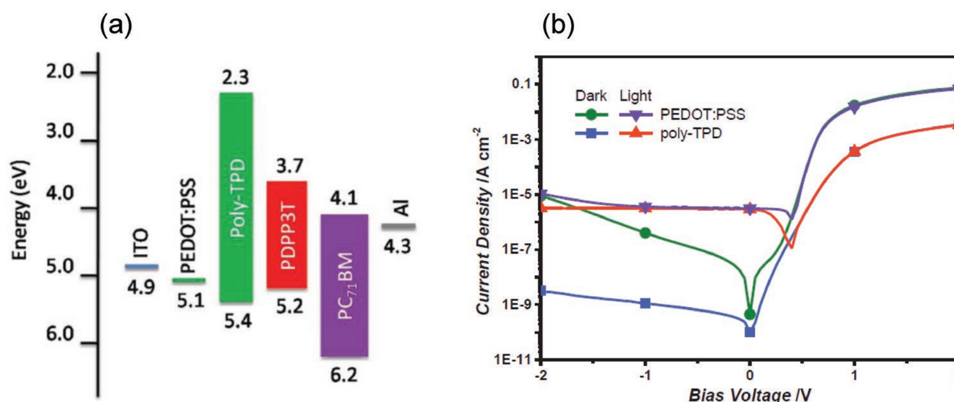

Figure 5. Effect of EBLs on the dark current density in BHJ OPDs. a) Energy band diagram of PDPP3T-based OPD, showing the superior electron-blocking properties of poly-TPD when compared to PEDOT:PSS due to the shallow LUMO energy. b) J–V characteristics of OPDs with PEDOT:PSS or poly-TPD EBL in dark conditions and under 850 nm monochromatic illumination (2.7 µW). Reproduced with permission.[35] Copyright 2015, Wiley-VCH Verlag GmbH & Co. KGaA.

demonstrated a 25 nm thick poly[N,N'-bis(4-butylphenyl)-N,N'-bisphenylbenzidine] (poly-TPD) EBL to suppress the reverse-bias dark current in an NIR OPD based on poly[[2,5-bis(2-hexyldecyl)-2,3,5,6-tetrahydro-3,6-dioxopyrrolo[3,4-c]-pyrrole-1,4-diyl]-alt-[2,2′:5′,2″-terthiophene]-5,5″-diyl] (PDPP3T) mixed with phenyl-C_{71}-butyric acid methyl ester ($PC_{71}BM$). Compared to the standard OPD with a PEDOT:PSS interlayer, introducing the poly-TPD EBL reduced the dark current density by more than two orders of magnitude due to the superior electron-blocking ability, leading to $J_d \approx 10^{-6}$ mA cm^{-2} under a reverse electric field of 6×10^6 V m^{-1} and thus a specific detectivity D^* greater than 1.0×10^{13} Jones at wavelengths from 350 to 870 nm. Although almost no loss in the EQE was reported under applied reverse bias, the small energy barrier of ≈ 0.2 eV at the interface between poly-TPD and the photoactive layer (**Figure 5**a) lowered the extraction efficiency near the V_{oc}, resulting in *s*-shaped J–V characteristics under illumination (Figure 5b). Nevertheless, poly-TPD was demonstrated to be a promising EBL material being a wide-bandgap hole transporting polymer with shallow LUMO level (–2.3 eV) and HOMO energy close to that of the donor polymer (PDPP3T).

4.3.2. Hole-Blocking Layers

In addition to EBLs, the use of polyethylenimine-ethoxylated (PEIE) as an effective HBL has been widely demonstrated. When a PEIE layer is solution-processed on the indium tin oxide (ITO) bottom electrode, simple aliphatic amine groups in this polymer are physisorbed onto the ITO and the CT nature of their interaction with the surface is found to reduce the ITO work function.[34] Therefore, the minimization of J_d in OPDs with PEIE interlayers is often attributed to its hole-blocking properties under reverse bias. Saracco et al.[50] first reported $J_d \approx 2 \times 10^{-6}$ mA cm^{-2} at $F = 6 \times 10^6$ V m^{-1} in OPDs consisting of a blend of poly[(4,8-bis-(2-ethylhexyloxy)-benzo(1,2-b:4,5-b′)dithiophene)-2,6-diyl-alt-(4-(2-ethylhexanoyl)-thieno[3,4-b]thiophene-)-2-6-diyl)] (PBDTTT-C) with $PC_{71}BM$, using PEIE interlayer. Pierre et al.[52] achieved an impressively low dark current density of 1.4×10^{-7} mA cm^{-2} and $D^* = 3.45 \times 10^{13}$ Jones using PCDTBT as donor polymer (**Figure 6**). Similarly, Kielar et al.[34] reached $J_d \approx 3 \times 10^{-7}$ mA cm^{-2} and $D^* = 3.21 \times 10^{13}$ Jones at ≈ 530 nm, which is amongst the highest reported specific detectivities at this wavelength.

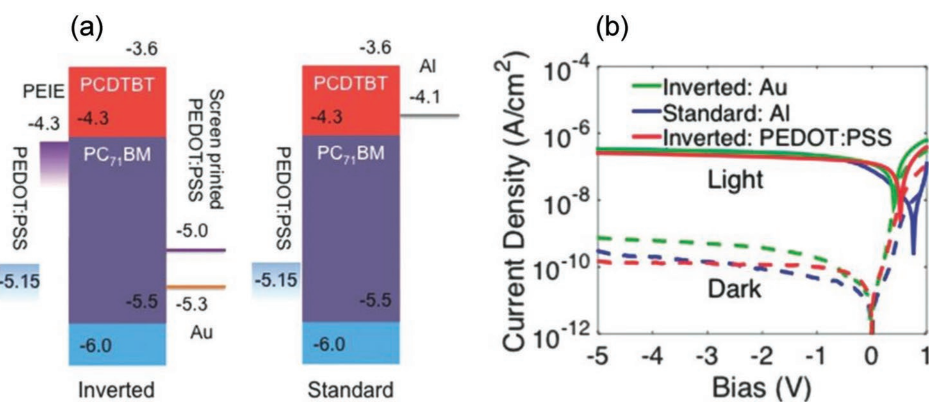

Figure 6. Effect of PEIE as HBL on the dark current density in BHJ OPDs. a) Energy band diagram for all-printed inverted OPD with PEIE interlayer and standard OPD with metal top contact. b) J–V characteristics in dark conditions and under illumination (532 nm, 1.03 µW cm^{-2}), showing the lowest J_d at $V = -5$ V for the all-printed OPD with PEIE interlayer. Reproduced with permission.[52] Copyright 2015, Wiley-VCH Verlag GmbH & Co. KGaA.

© 2019 The Authors. Published by WILEY-VCH Verlag GmbH & Co. KGaA, Weinheim

5. Exploring the Intrinsic Limits of the Dark Current in OPDs

In this section, we provide a quantitative analysis of two main dark current mechanisms, that is charge injection and bulk thermal generation. In the former case, we use an analytical model to show the dependence of the injection-limited J_d on the main material and device parameters, namely active layer thickness L, effective bandgap E_g, energetic disorder σ, and charge carrier mobility μ, all within a reasonable range for OPD applications. For the latter, we calculate the contribution from thermally generated carriers by treating the device as a blackbody, demonstrating that charge injection can be safely considered as the dominant contribution to J_d. Finally, based on this theoretical insight, we suggest guidelines to improve OPD performance.

5.1. Injection-Limited Dark Current

A major contributor to J_d, charge carrier injection under reverse bias proceeds via a thermally activated jump that promotes the injection of an electron (hole) from the Fermi level of the hole (electron) extracting electrode to a tail state in the acceptor LUMO (donor HOMO). We invoke the formalism proposed by Arkhipov et al.,[68] which captures the fundamental two-step process that contributes to the injection-limited dark current, namely a first carrier jump into the semiconductor followed by a certain probability to escape to the opposite electrode. This injection model considers 1) the image charge effect at the electrode, 2) the energetic site disorder inherent to organic semiconductors, and 3) the hopping charge transport mechanism. Charge injection occurs from the electrode Fermi level into tail states of the DOS of the active layer materials, as previously described by Gartstein and Conwell.[69] The charge carrier can escape recombination with its image charge under the conditions that a neighboring hopping site at equal or lower energy is encountered.[6] As the carrier moves away from the electrode interface, it drifts in the electric field towards the opposite electrode via a diffusive random walk in the disordered energetic landscape. It should be noted that the injection process will not be spatially homogeneous but instead filamentary,[70] since the first injection event is dominated by the presence of spatially fixed tail states in the DOS distribution close to the interfaces.

Applying the assumptions of the Arkhipov et al. formalism, we define the injection-limited J_d as the product between the charge carrier density at the metal–semiconductor interface n_{int} and the carrier mobility μ_0 in the bulk of the semiconductor:

$$J_d \propto q n_{int} \mu_0 F \tag{6}$$

Assuming a Gaussian DOS, the injection barrier Φ_{inj} is equal to Φ_b minus a term proportional to the thermal equilibrium energy, $\left(\frac{\sigma_i^2}{2k_BT}\right)$, with σ_i the energetic disorder at the metal–semiconductor interface. The effective Φ_{inj} is further reduced by the image potential barrier lowering $\Delta\Phi_b = \sqrt{\frac{qF}{4\pi\varepsilon}}$, being $\varepsilon = \varepsilon_0\varepsilon_r$ the permittivity. Under these conditions, $n_{int} = N_t \exp\left(-\frac{\Phi_{inj}}{k_BT}\right)$ with $\Phi_{inj} = \Phi_b - \left(\frac{\sigma_i^2}{2k_BT}\right) - \Delta\Phi_b$ (**Figure 7**a) and with N_t the volume density of molecular sites between which the hopping takes place. The mobility in the zero-field limit and at carrier density in the independent-particle (Boltzmann) regime μ_0 is equal to the product of the mobility in the infinite temperature limit, μ_0*, and a temperature-dependent factor $\exp\left[-C_i\left(\frac{\sigma_b}{k_BT}\right)^2\right]$, with σ_b the energetic disorder in the bulk of the semiconductor and $C_i \approx 0.4$ within the extended Gaussian density model.[71] Thus, the current density is given by:

$$J = A\, qN_t \exp\left[-\frac{\Phi_b - \left(\frac{\sigma_i^2}{2k_BT}\right) - \Delta\Phi_b}{k_BT}\right] \cdot \mu_0^* \exp\left[-C_i\left(\frac{\sigma_b}{k_BT}\right)^2\right] \cdot \frac{V}{L} \tag{7}$$

In this expression, the dimensionless prefactor A is considered equal to unity, as expected for OPDs with large injection barriers and uniform carrier density across the device thickness.[71]

The influence of the main OPD parameters on the injection-limited dark current under reverse bias voltage of $V = -3$ V as estimated from Equation (7) is shown in Figure 7b. Data are normalized to a reference case with $L = 100$ nm, $\mu_0 = 10^{-7}$ m^2 V^{-1} s^{-1}, $\Phi_b = 1$ eV, and $\sigma_i = 0.1$ eV. Each parameter is varied within a reasonable range for OPD applications while keeping the other parameters constant, thereby assuming their mutual independence. The V-dependence of J_d upon variations in L, μ_0, Φ_b, and σ_i is shown in Figure 7c–e, respectively.

The dark current density decreases with increasing active layer thickness, as observed in Section 4.2. However, the thickness dependence is weaker for increasing L, since J_d depends linearly on the electric field but exponentially on $\Delta\Phi_b$. Overall, the intrinsic thickness dependence of J_d is much less significant when compared to the other material parameters. However, very thick active layers ($\approx$ 800 nm) are beneficial in reducing J_d due to extrinsic effects, such as the reduction of pinholes and film imperfections,[5] as will be discussed in Section 6. For a single carrier, the dark current density depends linearly on the charge carrier mobility according to Equation (7). However, effective μ_0 below 10^{-9} m^2 V^{-1} s^{-1} for a charge carrier in a BHJ active layer is unrealistic, implying that μ_0 has limited importance in defining J_d. The major role in defining the injection-limited dark current density is played by the effective injection barrier, leading to a decrease by 5 orders of magnitude in J_d upon variations in Φ_b from 1.0 to only 1.3 eV. Remarkably, J_d increases by a factor 10 when the interface disorder σ_i is increased from 0.1 eV to only 0.12 eV, which underlines the importance of choosing active layer materials with low energetic disorder (such as PCBM).

5.2. Thermally Generated Dark Current

To determine whether bulk thermal generation makes a significant contribution to the dark current, we adapt an approach commonly applied to solar cells under illumination.[72,73] For solar cells, the short-circuit current J_{sc} is determined by the overlap integral between the incident photon flux, $\phi(E)$ and the external quantum efficiency spectrum, EQE(E) via

$$J_{sc} = q\int \mathrm{EQE}(E)\,\phi(E)\,dE \tag{8}$$

© 2019 The Authors. Published by WILEY-VCH Verlag GmbH & Co. KGaA, Weinheim

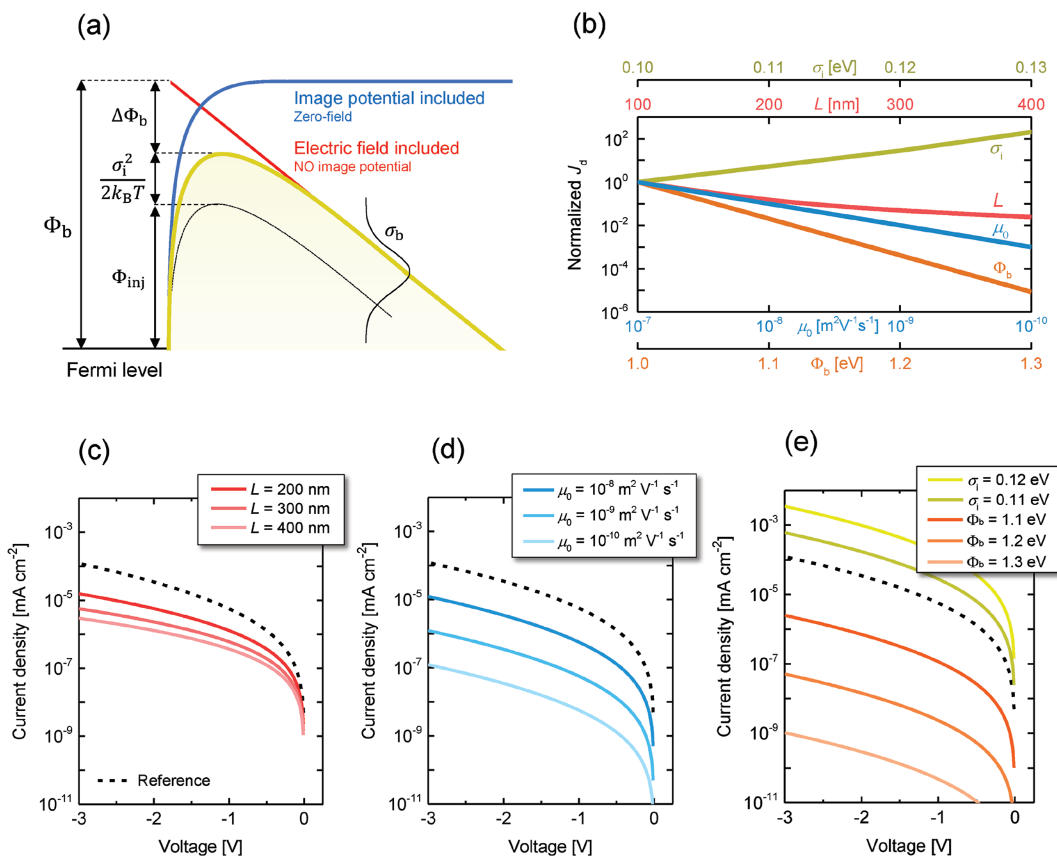

Figure 7. Injection-limited dark current calculations. a) Schematic of charge injection process from the electrode Fermi level into tail states of the semiconductor DOS. b) Influence of individual material parameters on the injection-limited J_d as calculated from Equation (7). The results are normalized to a reference case with $L = 100$ nm, $\mu_0 = 10^{-7}$ m^2 V^{-1} s^{-1}, $\Phi_b = 1$ eV, and $\sigma_i = 0.1$ eV. c) Effect of active layer thickness L, d) charge carrier mobility μ_0, e) effective injection barrier Φ_b and interface energetic disorder σ_i on the injection-limited J–V characteristics under reverse bias.

The thermally generated dark current can be calculated by replacing the typical AM1.5G solar spectrum with the blackbody spectrum. To determine the thermally generated photon flux, we begin with the well-known photon energy distribution $e(E)$ inside a blackbody in the interval from E to $E + dE$, given by

$$e(E)\,dE = \frac{8\pi}{h^3c^3}\frac{E^3}{\exp(E/k_BT)-1}dE \tag{9}$$

as taken from Vandewal et al.,[74] with c is the speed of light. Dividing by the energy of each photon E and a factor of c gives the photon flux emitted into a hemisphere from a planar unit surface, specifically

$$\phi(E)\,dE = \frac{2\pi}{h^3c^2}\frac{E^2}{\exp(E/k_BT)-1}dE \tag{10}$$

Multiplying by a factor of two to account for photon flux from both sides of the planar device, and converting to units of mA cm^{-2} eV^{-1}, gives the spectral photon flux over a range of temperatures (**Figure 8**a). Since for a blackbody emission and absorption are equivalent, the thermally generated J_d can simply be determined from Equation (8).

Three distinct variations to EQE spectra are made, specifically the maximum magnitude EQE_{max}, the optical bandgap E_0 and the energetic disorder σ. As for the injection-limited J_d, we define a reference case (black solid line) with $EQE_{max} = 0.1$, $E_0 = 0.12$ eV, and $\sigma = 0.1$ eV. The value of E_0 determines the edge of the EQE spectrum as defined in Figure S4 (Supporting Information). In particular, choosing $E_0 = 0.12$ eV enables a direct comparison with the reference OPD in Figure 7 ($\Phi_b = 0.1$ eV, therefore $E_g = 0.1$ eV in case of OPD with Ohmic contacts and without blocking layers), assuming energetic offset of 0.2 eV to achieve efficient CT from donor to acceptor.[63] As for the injection-limited J_d, two parameters are held constant while the influence of the other parameter on J_d is varied. Unsurprisingly, a larger EQE contribution at low energies increases the thermal dark current (Figure 8b), demonstrating the impact of sub-bandgap absorption. However, perhaps the most important point is that for a similar material parameter set, the injection-limited J_d (dotted line) is about 5 orders of magnitude above the thermally generated J_d (black solid line), meaning that charge injection can be regarded as the dominant contribution to the dark current density.

6. Why Does the Experimental J_d Deviate from its Intrinsic Limit?

Having explored the intrinsic limits of dark current density in Section 5, we now consider factors that may cause deviation of the experimental value from this calculated intrinsic lower limit. This deviation is illustrated by considering that a reference OPD

© 2019 The Authors. Published by WILEY-VCH Verlag GmbH & Co. KGaA, Weinheim

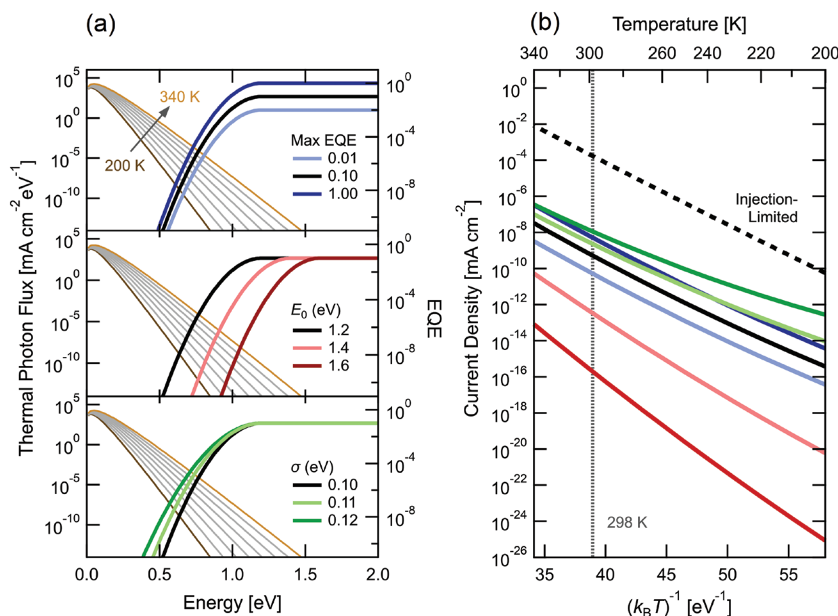

Figure 8. Thermally generated dark current calculations. a) Blackbody thermal photon flux $\phi(E)$ incident on a planar device, and hypothetical EQE spectra with various magnitudes, bandgaps E_0 and energetic disorders σ. b) The temperature-dependent dark current is determined from the overlap integral between EQE(E) and $\phi(E)$. The injection-limited dark current at $V = -3$ V for the reference case in Figure 7 is shown for comparison.

with typical parameters of $L = 100$ nm, $E_g = 1$ eV, $\mu_0 = 10^{-7}$ m^2 V^{-1} s^{-1}, and $\sigma_i = 0.1$ eV was calculated (at an effective electric field $F = 6 \times 10^6$ V m^{-1}) to have an intrinsic $J_d \approx 10^{-6}$ mA cm^{-2}, close to the empirical limit in Figure 3b assuming $E_g = 1$ eV. While a few data points in Figure 3b lie near the empirical limit, a clear majority of literature J_d values are significantly higher.

One explanation for this discrepancy lies in the experimental uncertainty in determining LUMO$_A$ and HOMO$_D$, as their absolute value can depend on the measurement technique.[75] As an example, the HOMO energy of PCDTBT was reported to be −5.5[52,34] or −5.4 eV.[13] Furthermore, reported LUMO energies of fullerene acceptors range between −4.3[52] and −3.8 eV.[13,75] While these uncertainties might affect the results in Figure 3b, they would not explain deviations from the J_d empirical limits by several orders of magnitude. Instead, in many cases J_d values are raised above the intrinsic limit by extrinsic factors, associated either with the OPD fabrication process or the J_d measurement protocol. Pinholes in the photoactive blend can lead locally to high current densities, especially for thinner layers. In some cases, lateral leakage current paths outside the active area effectively increase J_d. This effect can be studied by measuring OPDs with different active area and checking if J_d is independent of the active area. Similarly, local current density variation between the edge and the center of the device lead to area-dependent J_d values. Furthermore, displacement currents become non-negligible for state-of-the-art OPDs with low intrinsic dark currents, particularly around $V = 0$ V; such contributions can be ruled out ensuring that J_d is independent of the J–V scan rate and scan direction.

In addition, the dark current density in OPDs can be affected by energy states within the bandgap of the active layer, often referred to as traps. Close to the band edges (within ≈0.2 eV) lie tail states due to intrinsic energetic site disorder of organic materials[76] (quantified above with σ) that originate from variation in local microstructure. At similar energies lie extrinsic shallow traps, broadly attributed to chemical impurities such as oxygen, moisture and chemical impurities introduced during synthesis. Deep traps reside further into the bandgap,[77] attributed primarily to conjugation breaks, which are either due to synthetic defects or induced by impurities.[57] The precise origin of trap states is a topic of extensive ongoing discussion, with a universal trap level at around −3.6 eV identified in 2012 for a variety of conjugated polymers and attributed to the formation of hydrated oxygen complexes.[78] More recent

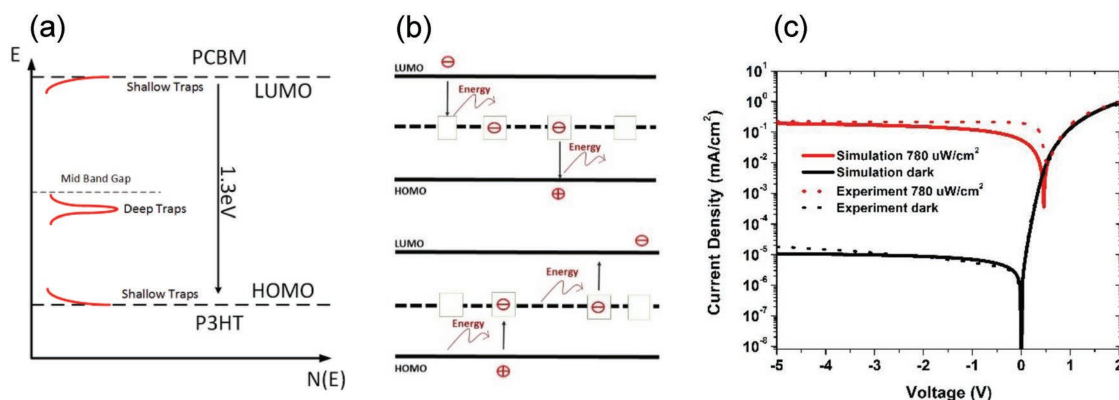

Figure 9. Effect of trap states on J_d in BHJ OPDs. a) Schematic representation of shallow and deep trap densities of states. b) Trap-mediated recombination and generation processes within the photoactive layer. c) Good agreement between experimental and simulated J–V characteristics in dark and under illumination is obtained only considering the effect of traps on the OPD charge injection and transport properties. Reproduced with permission.[57] Copyright 2017, Institute of Electrical and Electronics Engineers.

© 2019 The Authors. Published by WILEY-VCH Verlag GmbH & Co. KGaA, Weinheim

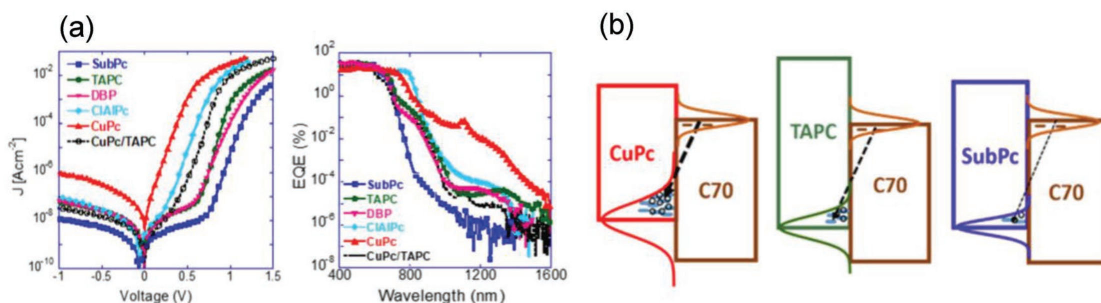

Figure 10. Effect deep subgap states on J_d in PHJ OPDs. a) Correlation between reverse-bias dark current density and strength of the signature of subgap states in the EQE spectra. c) Schematic representation of the physical mechanisms occurring at the D-A interface using different donor materials in combination with C_{70} acceptor. Reproduced with permission.[39] Copyright 2017, American Institute of Physics.

works[79,80] support this attribution to moisture, suggesting that water molecules are present in voids within the active layer, even when the device is processed under notionally inert conditions, with Zuo et al.[81] recently demonstrating that they lie ≈0.3–0.4 eV above and below the HOMO and LUMO levels, respectively.

Regardless of their origin, both shallow traps/tail states and deep traps can enhance J_d by both reducing the energetic jump required for charge injection and increasing the density of thermally generated carriers, since random thermal excitations cause electrons to jump to an unoccupied trap level and subsequently to the acceptor LUMO. Indeed, Fallahpour et al.[57] demonstrated that deep trap states within the photoactive layer can influence the transport mechanism of the OPD due to trap-mediated capture and emission of electrons from/into the HOMO and LUMO levels (**Figure 9**a,b). Using a drift-diffusion model to simulate the dark current density of a P3HT:PC_{61}BM OPD, excellent agreement with the experimental J–V characteristics was obtained assuming the presence of deep and shallow traps (Figure 9c). This underlines the importance of designing photoactive materials with as low trap densities as possible to achieve high sensitivity OPDs.

Shekhar et al.[39] studied the effect of deep subgap states on the dark current density of PHJ OPDs. Measuring EQE spectra extended up to 1600 nm, the presence of subgap states and/or defect-induced states in the proximity of the D-A interface was investigated. The reduction in J_d on exchanging copper phthalocyanine (CuPc) for TAPC and then for boron SubPc chloride was attributed to the smaller tail state density, and thus lower charge generation/recombination rate at the D-A interface (**Figure 10**). This suggests that the dark current density can be effectively reduce by minimizing the density of deep sub-gap states at the D-A junction.

In addition to J_d, extrinsic trap states were found to affect other OPD metrics such as the absolute EQE and the speed of response (see Sections 2.1 and 2.2). Cowan et al.[82] quantified the role of traps in a PCDTBT:PC_{61}BM BHJ solar cell by adding PC_{84}BM as a well-defined trap state impurity. The addition of PC_{84}BM decreased the efficiency of photon-to-electron conversion, thereby decreasing the EQE. Furthermore, trap states at the electrode–semiconductor interface were found to be the main cause of the persistent photoconductivity behavior,[83] decreasing the speed of response. In OPDs, these interface traps can originate if the HEL or EEL leads to oxidation of adjacent species, as it was identified for PEDOT-PSS.[84] Water and oxygen must thus be excluded from the OPD to ensure stability and durability.[85] Therefore, commercial OPDs often demand thin-film encapsulation[86] and suitable device architecture[87] to achieve viable lifetimes.

7. Conclusion

In summary, OPDs offer significant advantages over conventional inorganic photodetectors, most notably flexibility and bandgap tunability, which potentially facilitate new applications. Achieving sufficiently high-performance metrics requires lowering J_d as much as possible. An overview of dark current densities reported in recent years shows a large spread in J_d values that merits further analysis. We identified charge injection from the contacts into the semiconductor as the dominant intrinsic contribution to J_d and we found that state-of-the-art OPDs are close to the expected intrinsic limit. Thus, once extrinsic contributions such as leakage are eliminated, for a given effective bandgap, the dark current density can be reduced by minimizing the active layer energetic disorder and trap state density.

Acknowledgements

The research received funding from the Ministry of Education, Culture and Science (Gravity program 024.001.035). M.D. thanks the Marie Skłodowska-Curie Actions Innovative Training Network "H2020-MSCAITN-2014 INFORM—675867" for financial support.

Conflict of Interest

The authors declare no conflict of interest.

Keywords

bulk heterojunction, dark current, image sensors, organic photodetectors, traps

Received: May 26, 2019
Revised: August 10, 2019
Published online:

[1] R. D. Jansen-van Vuuren, A. Armin, A. K. Pandey, P. L. Burn, P. Meredith, *Adv. Mater.* **2016**, *28*, 4766.
[2] K. Baeg, M. Binda, D. Natali, M. Caironi, Y. Noh, *Adv. Mater.* **2013**, *25*, 4267.

 © 2019 The Authors. Published by WILEY-VCH Verlag GmbH & Co. KGaA, Weinheim

[3] T. Someya, Y. Kato, S. Iba, Y. Noguchi, T. Sekitani, H. Kawaguchi, T. Sakurai, *IEEE Trans. Electron Devices* **2005**, *52*, 2502.
[4] R. A. Street, I. Fujieda, R. Weisfield, S. Nelson, P. Nylen, *MRS Proc.* **1992**, *258*, 1145.
[5] M. Biele, C. Montenegro Benavides, J. Hürdler, S. F. Tedde, C. J. Brabec, O. Schmidt, *Adv. Mater. Technol.* **2019**, *4*, 1800158.
[6] A. Köhler, H. Bässler, *Electronic Processes in Organic Semiconductors*, Wiley-VCH, Weinheim **2015**.
[7] M. C. Scharber, N. S. Sariciftci, *Prog. Polym. Sci.* **2013**, *38*, 1929.
[8] Y. Huang, E. J. Kramer, A. J. Heeger, G. C. Bazan, *Chem. Rev.* **2014**, *114*, 7006.
[9] P. Zalar, N. Matsuhisa, T. Suzuki, S. Enomoto, M. Koizumi, T. Yokota, M. Sekino, T. Someya, *Adv. Electron. Mater.* **2018**, *4*, 1700601.
[10] Y. L. Wu, N. Matsuhisa, P. Zalar, K. Fukuda, T. Yokota, T. Someya, *Adv. Electron. Mater.* **2018**, *4*, 1800311.
[11] T. N. Ng, W. S. Wong, M. L. Chabinyc, S. Sambandan, R. A. Street, *Appl. Phys. Lett.* **2008**, *92*, 213303.
[12] C. Zhao, J. Kanicki, A. C. Kostantinidis, T. Patel, *Med. Phys.* **2015**, *42*, 6294.
[13] G. H. Gelinck, A. Kumar, D. Moet, J. P. J. Van Der Steen, A. J. J. M. Van Breemen, S. Shanmugam, A. Langen, J. Gilot, P. Groen, R. Andriessen, M. Simon, W. Ruetten, A. U. Douglas, R. Raaijmakers, P. E. Malinowski, K. Myny, *IEEE Trans. Electron Devices* **2016**, *63*, 197.
[14] T. Kamada, R. Hatsumi, K. Watanabe, S. Kawashima, M. Katayama, H. Adachi, T. Ishitani, K. Kusunoki, D. Kubota, S. Yamazaki, *J. Soc. Inf. Disp.* **2019**, *27*, 361.
[15] H. Akkerman, B. Peeters, A. van Breemen, S. Shanmugam, D. Tordera, J.-L. van der Steen, A. J. Kronemeijer, P. Malinowski, F. De Roose, D. Cheyns, J. Genoe, W. Dehaene, P. Heremans, G. Gelinck, *SID Symp. Dig. Tech. Pap.* **2018**, *49*, 494.
[16] C. M. Lochner, Y. Khan, A. Pierre, A. C. Arias, *Nat. Commun.* **2014**, *5*, 5745.
[17] Y. Khan, D. Han, A. Pierre, J. Ting, X. Wang, C. M. Lochner, G. Bovo, N. Yaacobi-Gross, C. Newsome, R. Wilson, A. C. Arias, *Proc. Natl. Acad. Sci. USA* **2018**, *115*, E11015.
[18] T. Morimune, H. Kajii, Y. Ohmori, *IEEE Photon. Technol. Lett.* **2006**, *18*, 2662.
[19] Holst Centre, imec and Philips demo world's first curved, plastic photodetector, https://www.holstcentre.com/news—press/2017/curvedxray/, (accessed:May 2019).
[20] Magic Pad in Organic Electronics Association (OE-A) brochure, http://www.isorg.fr/actu/8/magic-pad-in-organic-electronics-association-oe-a-brochure_69.htm, (accessed: May 2019).
[21] A. Armin, R. D. Jansen-Van Vuuren, N. Kopidakis, P. L. Burn, P. Meredith, *Nat. Commun.* **2015**, *6*, 6343.
[22] B. Siegmund, A. Mischok, J. Benduhn, O. Zeika, S. Ullbrich, F. Nehm, M. Böhm, D. Spoltore, H. Fröb, C. Körner, K. Leo, K. Vandewal, *Nat. Commun.* **2017**, *8*, 15421.
[23] S. Ullbrich, B. Siegmund, A. Mischok, A. Hofacker, J. Benduhn, D. Spoltore, K. Vandewal, *J. Phys. Chem. Lett.* **2017**, *8*, 5621.
[24] Z. Tang, Z. Ma, A. Sánchez-Díaz, S. Ullbrich, Y. Liu, B. Siegmund, A. Mischok, K. Leo, M. Campoy-Quiles, W. Li, K. Vandewal, *Adv. Mater.* **2017**, *29*, 1702184.
[25] M. R. Esopi, M. Calcagno, Q. Yu, *Adv. Mater. Technol.* **2017**, *2*, 1700025.
[26] N. Strobel, R. Eckstein, J. Lehr, U. Lemmer, G. Hernandez-Sosa, *Adv. Electron. Mater.* **2018**, *4*, 1700345.
[27] S. A. Choulis, J. Nelson, Y. Kim, D. Poplavskyy, T. Kreouzis, J. R. Durrant, D. D. C. Bradley, *Appl. Phys. Lett.* **2003**, *83*, 3812.
[28] G. Garcia-Belmonte, A. Munar, E. M. Barea, J. Bisquert, I. Ugarte, R. Pacios, *Org. Electron.* **2008**, *9*, 847.
[29] T. M. Clarke, C. Lungenschmied, J. Peet, N. Drolet, A. J. Mozer, *Adv. Energy Mater.* **2015**, *5*, 1401345.
[30] S. Kasap, J. B. Frey, G. Belev, O. Tousignant, H. Mani, J. Greenspan, L. Laperriere, O. Bubon, A. Reznik, G. DeCrescenzo, K. S. Karim, J. A. Rowlands, *Sensors* **2011**, *11*, 5112.
[31] G. A. H. Wetzelaer, M. Kuik, M. Lenes, P. W. M. Blom, *Appl. Phys. Lett.* **2011**, *99*, 153506.
[32] T. Martin, R. Landauer, *Phys. Rev. B* **1992**, *45*, 1742.
[33] I. K. Kim, J. H. Jo, J. Lee, Y. J. Choi, *Org. Electron.* **2018**, *57*, 89.
[34] M. Kielar, O. Dhez, G. Pecastaings, A. Curutchet, L. Hirsch, *Sci. Rep.* **2016**, *6*, 39201.
[35] X. Zhou, D. Yang, D. Ma, *Adv. Opt. Mater.* **2015**, *3*, 1570.
[36] P. E. Keivanidis, P. K. H. Ho, R. H. Friend, N. C. Greenham, *Adv. Funct. Mater.* **2010**, *20*, 3895.
[37] H. Yoshida, *J. Phys. Chem. C* **2014**, *118*, 24377.
[38] S. Yoon, J. Ha, J. Cho, D. S. Chung, *Adv. Opt. Mater.* **2016**, *4*, 1933.
[39] H. Shekhar, O. Solomeshch, D. Liraz, N. Tessler, *Appl. Phys. Lett.* **2017**, *111*, 223301.
[40] T. Agostinelli, M. Campoy-Quiles, J. C. Blakesley, R. Speller, D. D. C. Bradley, J. Nelson, *Appl. Phys. Lett.* **2008**, *93*, 203305.
[41] H. Wang, S. Xing, Y. Zheng, J. Kong, J. Yu, A. D. Taylor, *ACS Appl. Mater. Interfaces* **2018**, *10*, 3856.
[42] S. Yoon, J. Cho, K. M. Sim, J. Ha, D. S. Chung, *Appl. Phys. Lett.* **2017**, *110*, 083301.
[43] N. Gasparini, A. Gregori, M. Salvador, M. Biele, A. Wadsworth, S. Tedde, D. Baran, I. McCulloch, C. J. Brabec, *Adv. Mater. Technol.* **2018**, *3*, 1800104.
[44] E. S. Zaus, S. Tedde, J. Fürst, D. Henseler, G. H. Döhler, *J. Appl. Phys.* **2007**, *101*, 044501.
[45] M. Ramuz, L. Bürgi, C. Winnewisser, P. Seitz, *Org. Electron.* **2008**, *9*, 369.
[46] M. Binda, A. Iacchetti, D. Natali, L. Beverina, M. Sassi, M. Sampietro, *Appl. Phys. Lett.* **2011**, *98*, 073303.
[47] S. Valouch, C. Hönes, S. W. Kettlitz, N. Christ, H. Do, M. F.G. Klein, H. Kalt, A. Colsmann, U. Lemmer, *Org. Electron.* **2012**, *13*, 2727.
[48] F. Guo, Z. Xiao, J. Huang, *Adv. Opt. Mater.* **2013**, *1*, 289.
[49] F. Arca, M. Sramek, S. F. Tedde, P. Lugli, O. Hayden, *IEEE J. Quantum Electron.* **2013**, *49*, 1016.
[50] E. Saracco, B. Bouthinon, J. Verilhac, C. Celle, N. Chevalier, D. Mariolle, O. Dhez, J. Simonato, *Adv. Mater.* **2013**, *25*, 6534.
[51] I. K. Kim, X. Li, M. Ullah, P. E. Shaw, R. Wawrzinek, E. B. Namdas, S. Lo, *Adv. Mater.* **2015**, *27*, 6390.
[52] A. Pierre, I. Deckman, P. B. Lechêne, A. C. Arias, *Adv. Mater.* **2015**, *27*, 6411.
[53] A. Grimoldi, L. Colella, L. La Monaca, G. Azzellino, M. Caironi, C. Bertarelli, D. Natali, M. Sampietro, *Org. Electron.* **2016**, *36*, 29.
[54] X. Wang, J. Huang, J. Li, J. Yu, *J. Phys. D: Appl. Phys.* **2016**, *49*, 075102.
[55] S. Bin Lim, C. H. Ji, K. T. Kim, S. Y. Oh, *J. Korean Phys. Soc.* **2016**, *69*, 421.
[56] I. K. Kim, J. H. Jo, *IEEE Sens. J.* **2016**, *16*, 4767.
[57] A. H. Fallahpour, S. Kienitz, P. Lugli, *IEEE Trans. Electron Devices* **2017**, *64*, 2649.
[58] J. U. Ha, K. Kim, S. Yoon, K. M. Sim, J. Cho, D. S. Chung, *ACS Photonics* **2017**, *4*, 2085.
[59] S. H. Eom, S. Y. Nam, H. J. Do, J. Lee, S. Jeon, T. J. Shin, I. H. Jung, S. C. Yoon, C. Lee, *Polym. Chem.* **2017**, *8*, 3612.
[60] C. M. Benavides, P. Murto, C. L. Chochos, V. G. Gregoriou, A. Avgeropoulos, X. Xu, K. Bini, A. Sharma, M. R. Andersson, O. Schmidt, C. J. Brabec, E. Wang, S. F. Tedde, *ACS Appl. Mater. Interfaces* **2018**, *10*, 12937.
[61] C. C. Lee, S. Biring, S. J. Ren, Y. Z. Li, M. Z. Li, N. R. Al Amin, S. W. Liu, *Org. Electron.* **2019**, *65*, 150.
[62] J. Qi, W. Qiao, X. Zhou, D. Yang, J. Zhang, D. Ma, Z. Y. Wang, *Macromol. Chem. Phys.* **2016**, *217*, 1683.
[63] M. C. Scharber, D. Mühlbacher, M. Koppe, P. Denk, C. Waldauf, A. J. Heeger, C. J. Brabec, *Adv. Mater.* **2006**, *18*, 789.

© 2019 The Authors. Published by WILEY-VCH Verlag GmbH & Co. KGaA, Weinheim

[64] J. B. Park, J. W. Ha, S. C. Yoon, C. Lee, I. H. Jung, D. H. Hwang, *ACS Appl. Mater. Interfaces* **2018**, *10*, 38294.
[65] T. Van Woudenbergh, *Charge Injection into Organic Semiconductors, PhD Thesis*, Groningen University, **2005**.
[66] S. F. Tedde, J. Kern, T. Sterzl, J. Fürst, P. Lugli, O. Hayden, *Nano Lett.* **2009**, *9*, 980.
[67] Z. Wu, W. Yao, A. E. London, J. D. Azoulay, T. N. Ng, *ACS Appl. Mater. Interfaces* **2017**, *9*, 1654.
[68] V. I. Arkhipov, U. Wolf,, H. Bässler, *Phys. Rev. B* **1999**, *59*, 7514.
[69] Y. N. Gartstein, E. M. Conwell, *Chem. Phys. Lett.* **1995**, *245*, 351.
[70] J. J. M. Van Der Holst, M. A. Uijttewaal, B. Ramachandhran, R. Coehoorn, P. A. Bobbert, G. A. de Wijs, R. A. de Groot, *Phys. Rev. B* **2009**, *79*, 085203.
[71] W. F. Pasveer, J. Cottaar, C. Tanase, R. Coehoorn, P. A. Bobbert, P. W. M. Blom, D. M. de Leeuw, M. A. J. Michels, *Phys. Rev. Lett.* **2005**, *94*, 206601.
[72] Y. Liang, Z. Xu, J. Xia, S. T. Tsai, Y. Wu, G. Li, C. Ray, L. Yu, *Adv. Mater.* **2010**, *22*, E135.
[73] M. Padilla, B. Michl, B. Thaidigsmann, W. Warta, M.C. Schubert, *Sol. Energy Mater. Sol. Cells* **2014**, *120*, 282.
[74] K. Vandewal, K. Tvingstedt, J. V. Manca, O. Inganäs, *IEEE J. Sel. Top. Quantum Electron.* **2010**, *16*, 1676.
[75] R. E. M. Willems, L. C. H. Weijtens, X. de Vries, R. Coehoorn, R. A. J. Janssen, *Adv. Energy Mater.* **2019**, *9*, 1803677.
[76] D. Venkateshvaran, M. Nikolka, A. Sadhanala, V. Lemaur, M. Zelazny, M. Kepa, M. Hurhangee, A. J. Kronemeijer, V. Pecunia, I. Nasrallah, I. Romanov, K. Broch, I. McCulloch, D. Emin, Y. Olivier, J. Cornil, D. Beljonne, H. Sirringhaus, *Nature* **2014**, *515*, 384.
[77] J. A. Carr, S. Chaudhary, *Energy Environ. Sci.* **2013**, *6*, 3414.
[78] H. T. Nicolai, M. Kuik, G. A. H. Wetzelaer, B. de Boer, C. Campbell, C. Risko, J. L. Brédas, P. W. M. Blom, *Nat. Mater.* **2012**, *11*, 882.
[79] M. Nikolka, I. Nasrallah, B. Rose, M. K. Ravva, K. Broch, A. Sadhanala, D. Harkin, J. Charmet, M. Hurhangee, A. Brown, S. Illig, P. Too, J. Jongman, I. McCulloch, J. L. Bredas, H. Sirringhaus, *Nat. Mater.* **2017**, *16*, 356.
[80] M. Nikolka, G. Schweicher, J. Armitage, I. Nasrallah, C. Jellett, Z. Guo, M. Hurhangee, A. Sadhanala, I. McCulloch, C. B. Nielsen, H. Sirringhaus, *Adv. Mater.* **2018**, *30*, 1801874.
[81] G. Zuo, M. Linares, T. Upreti, M. Kemerink, *Nat. Mater.* **2019**, *18*, 588.
[82] S. R. Cowan, W. L. Leong, N. Banerji, G. Dennler, A. J. Heeger, *Adv. Funct. Mater.* **2011**, *21*, 3083.
[83] O. Katz, G. Bahir, J. Salzman, *Appl. Phys. Lett.* **2004**, *84*, 4092.
[84] F. Arca, S. F. Tedde, M. Sramek, J. Rauh, P. Lugli, O. Hayden, *Sci. Rep.* **2013**, *3*, 1324.
[85] M. Stevens, S. Tuomela, D. Mayer, In *Proceedings of the Society of Vacuum Coaters*, 48th Annual Technical Conference Proceedings, April 23–28, **2005**. Denver, Colorado, p. 189.
[86] R. Satoh, T. Ro, C. J. Heo, G. H. Lee, W. Xianyu, Y. Park, J. Park, S. J. Lim, D. S. Leem, X. Bulliard, Y. Kim, K. Bae, W. Y. Yang, K. B. Park, Y. W. Jin, S. Lee, *Org. Electron.* **2017**, *41*, 259.
[87] D. Zhao, M. Wu, R. Qin, J. Yu, *Opt. Lett.* **2018**, *43*, 3212.

© 2019 The Authors. Published by WILEY-VCH Verlag GmbH & Co. KGaA, Weinheim